35th AIAA Fluid Dynamics Conference, June 6–9, Toronto, Ontario

# Analysis and Control of Transonic Cavity Flow Using DES and LES

P. Nayyar,* G. N. Barakos,† K. J. Badcock‡
*University of Glasgow, Glasgow, G12 8QQ, UK*

D. A. Kirkham§
*BAE SYSTEMS, Warton, Preston, Lancashire, PR41AX, UK*

**Numerical simulations of the flow inside a cavity with a length-to-depth ratio (L/D) of 5 and a width-to-depth ratio (W/D) of 1 have been conducted using Large-Eddy Simulation (LES) and Detached-Eddy Simulation (DES). The cavity is exposed to a free-stream of zero incidence, $M_\infty = 0.85$ and $Re = 1 \times 10^6$ (based on the cavity length). Previous numerical simulations of 3D cavities using Unsteady Reynolds-Averaged Navier-Stokes (URANS) have proved difficult in accurately predicting the noise level and frequency content (and hence flow features) inside cavities. Simulation techniques such as LES and DES are therefore applied to the 3D cavity and this paper demonstrates its superior effectiveness relative to URANS in the analysis of cavity flows. Plots depicting the level of noise, frequency content and velocity profiles inside the cavity are presented. Comparisons are made with experimental unsteady pressure and PIV measurements. It was found that both DES and LES fare much better than URANS in resolving the higher frequencies and velocity distributions inside the cavity.**

## Nomenclature

| | |
|---|---|
| $A$ | Cross-sectional area |
| $D$ | Cavity depth |
| $dt$ | CFD time-step |
| $h$ | Height of control device |
| $L$ | Cavity length |
| $LE$ | Cavity leading-edge (lip) |
| $M$ | Mach number |
| $Re$ | Reynolds number, $R_e = \frac{UL}{\nu}$ |
| $SPL$ | Sound Pressure Level |
| $TE$ | Cavity trailing-edge (downstream corner) |
| $U$ | Velocity |
| $W$ | Cavity width |
| $w$ | Width of control device |
| $x$,$y$,$z$ | X-, y- and z- coordinates |

*Subscripts*

| | |
|---|---|
| $\infty$ | Free-stream |
| $rms$ | Root-mean square value |
| j | Jet |

*PhD Student, CFD Laboratory, Department of Aerospace Engineering. pnayyar@aero.gla.ac.uk.
†Lecturer, CFD Laboratory, Department of Aerospace Engineering.
‡Reader, CFD Laboratory, Department of Aerospace Engineering.
§Senior Aerodynamicist, BAE SYSTEMS, Warton Aerodrome

| | |
|---|---|
| sp | Spoiler |

*Symbols*

| | |
|---|---|
| $\alpha$,$\beta$,$\sigma_k$,$\sigma_\omega$ | Model coefficients |
| $\beta^*$ | Coefficient for the $k-\omega$ model |
| $\Delta$ | Metric of the grid size |
| $\nu$ | Kinematic viscosity |
| $\omega$ | Turbulent dissipation rate specific to turbulent kinetic energy |
| $\rho$ | Density |
| $\varepsilon$ | Turbulent dissipation rate |
| $a$,$b$ | Arbitrary parameters |
| $C_\mu$ | Jet blowing coefficient, $C_\mu = \frac{U_j A_j}{U_\infty A}$ |
| $C_{DES}$ | DES constant |
| $C_{w1}$,$f_{w1}$ | Functions for the Spalart-Allmaras model |
| $d$ | Distance to the nearest wall |
| $f_1$ | Blending function |
| $F_2$ | Vorticity-dependent shear stress limiter for the SST model |
| $k$ | Turbulent kinetic energy |
| $l$ | Turbulent length scale |
| $p$ | Pressure |
| $y$,$y_n$ | Distance normal to wall |

## Introduction

Ever since the introduction of internal store carriage, the need to understand cavity flows has been paramount. Carrying stores inside a weapons bay embedded in the aircraft's fuselage has significant advantages such as reduced aerodynamic heating of the store, reduced aircraft drag, enhanced manoeuvrability and reduced radar cross-section of the aircraft. However, when the weapon bay doors are opened to release the store, exposure of the cavity to the free-stream has been found to generate undesirable effects. Where the cavity length-to-depth (L/D) ratio is large, the flow separates and expands as it flows past the cavity lip, re-attaches at the cavity floor and then separates and compresses before the downstream wall. Low pressure and high pressure regions of recirculation develop at the front and rear walls of the cavity and the flow is said to be 'closed'. In this situation, although the flow is less unsteady, a differential pressure forms along the cavity longitudinal axis creating large pitching moments that can have adverse effects on the proper release of the store. As the cavity L/D ratio is reduced, the lower and higher pressure recirculation regions at the front and rear of the closed cavity merge resulting in a more uniform longitudinal pressure distribution and hence more benign store release and separation characteristics. The cavity flow in this case is classified as 'open'. Depending on the free-stream Mach number and the oncoming boundary layer thickness, however, the shear layer impinges on the cavity downstream wall generating acoustical disturbances. Reflections of the resulting pressure waves off the cavity walls and interactions with the shear layer instigates further instabilities in the flow. Self-sustained pressure oscillations result and the flow becomes highly unsteady and turbulent yielding very high noise levels and frequencies. The resultant noise spectrum is typically composed of discrete acoustic tones super-imposed on a broadband signature and can have damaging consequences on the structure surrounding the cavity and on the sensitive equipment that may be housed inside the cavity. The need to suppress these noise levels is therefore vital if the proper function of the store, for instance, is to be ensured. Before weapons bay flow control mechanisms can be adopted and the design methodologies of weapons bay improved, it is imperative to understand the physical mechanisms that drive the flow inside the cavity.

Investigations into the flow physics of cavities were conducted initially by Rossiter,[1] among others, in the 1960s at the Royal Aircraft Establishment. He performed numerous wind tunnel experiments and developed a semi-empirical formula to predict the frequencies produced in the cavity. In the subsequent years from Rossiter, numerous experiments have been performed and different theoretical models devised primarily to further the understanding of the physics of cavity flows, the acoustics generated and its suppression.[2,3,4,5] Further advances in the experimental front in the recent years, has seen the application of less intrusive and more accurate high-resolution methods such as Particle Image Velocimetry (PIV) and Laser Doppler Anemometry (LDV) to cavity flows.[6,7] Such modern experimental methods are however either expensive

or rarely available. Combined with rising wind tunnel costs, efforts in the last decade have therefore been made toward using Computational Fluid Dynamics (CFD) as an analysis tool for cavity flows.

Although numerical analysis of cavities have been conducted over a variety of different flow and geometric configurations, most have concentrated on cavity flows in the supseronic regime.[8,9,10] Furthermore, most of the numerical analysis of cavity flows has involved using the Reynolds-Averaged Navier-Stokes (RANS) equations. This requires the use of turbulence models to resolve the mean flow and turbulence properties. A significant proportion of these analyses have employed simple algebraic turbulence models,[11] typically for supersonic flows. More advanced turbulence models such as one-equation[12] and two-equation models[13] have also been applied to subsonic and transonic speeds in both 2D and 3D cavity flows but with limited success, as was also reported by Tam in Ref. 11.

In light of the difficulties associated with the turbulence modelling of cavity flows, some current research has looked at the simulation of cavity flows via methods such as Large-Eddy Simulation (LES).[14,15,16] LES works by filtering the flow structures in terms of scale size, with the larger scales explicitly resolved and the much smaller ones modelled using a sub-grid scale (SGS) model. With a significantly lower proportion of the flow modelled compared to Unsteady Reynolds-Averaged Navier-Stokes (URANS) methods, LES solutions are potentially more useful. For high Reynolds number flows, however, LES is expensive. Recent endeavours have therefore looked at developing hybrids of URANS and LES to obtain the best of both methods. One example of such developments includes Detached-Eddy Simulation (DES) introduced by Spalart.[17] Although Shieh, Hamed and Vishwanathan in Refs. 12, 18, 19 respectively have all reported good success with DES to resolve the cavity flow characteristics, their works have however focussed on either flow speeds greater or lower and at Reynolds numbers typically lower than those investigated here.

This paper focuses on how CFD can be used for the analysis and control of the flow field inside a weapons bay, building on the experiments performed by Ross of QinetiQ.[20] The experiment considered a clean, open rectangular cavity with a length-to-depth ratio (L/D) of 5 and a width-to-depth ratio (W/D) of 1 with doors-on and doors-off. The flow conditions correspond to a Mach number of 0.85 and a Reynolds number of 6.783 million based on the cavity length. A variety of turbulence modelling and simulation techniques have been used, including LES and DES. Computations have been performed with the Parallel Multi-Block (PMB) code developed at the University of Glasgow. Numerical results are compared with wind tunnel measurements along the cavity floor to illustrate the noise level and frequency content inside the cavity. PIV measurements were also provided by Ross[a] and this was also used to compare the velocity distribution inside the cavity predicted by CFD.

Application of different turbulence modelling and simulation techniques to cavity flows enabled a better understanding of the physical mechanisms that drive the flow in cavities to be acquired. Efforts were then undertaken to investigate different methods to control the highly unsteady and turbulent cavity environment. Cavity flow control has always received significant attention and the large volume of papers in literature discussing different passive and active control methods is a testament to this. Ross & Peto[21] have also conducted significant experiments in mitigating the harsh aero-acoustic cavity environment. They investigated both passive control devices that manipulated the cavity geometry either directly (for instance by shaping cavity walls) or indirectly (for instance by adding spoilers outside the cavity). In the recent years, active control methods are being to receive more attention because they tend to be more versatile across a greater proportion of the flight envelope. Cattafesta *et al.* in Ref. 22, for example, provide an elaborate account of different open-loop and closed-loop control strategies adopted by different researchers.

Although flow control of cavities of greater L/D ratio is likely to be also required to, for instance, suppress the large pitching moments for better store release characteristics, emphasis on mitigating the large noise levels and high frequencies encountered in the L/D=5 cavity is only addressed here. A preliminary study using passive control devices was conducted for the 2D L/D=5 cavity using the SST turbulence model. The SST model was found to provide reasonable accuracy (especially on coarse grids) out of all the turbulence models investigated in previous analyses and so was applied for this flow control study. Although DES computations were not performed in order to reduce computational run-time, further work will look at applying DES to study the flow control aspect of the open cavity flow. Even though no experimental data was available for this study, the basis of the flow control study performed builds on the experiments conducted by Ross & Peto[21] in DERA Bedford. Effects of the spoiler, slanted cavity walls and steady jet blowing on the cavity flow environment are illustrated. Comparisons were made with numerical and experimental results corresponding to the default cavity configuration where no control device is used to illustrate the effectiveness

[a]Private Communication

of the control method.

## Mathematical Model

### CFD Solver

All computations were performed using the Parallel Multi-Block (PMB) flow solver[23] developed at the University of Glasgow, which has been continually revised and updated over a number of years. The solver has been successfully applied to a variety of problems including cavity flows, hypersonic film cooling, spiked bodies, flutter and delta wing flows amongst others.

The code solves the unsteady Reynolds Averaged Navier-Stokes equations on multi-block structured grids, in serial or parallel mode. Governing equations are discretised using a cell-centred finite volume method. The convective terms are discretised using either Osher's or Roe's scheme. MUSCL interpolation is used to provide nominally third order accuracy and the Van Albada limiter is used to avoid spurious oscillations across shocks. The time-marching of the solution is based on an implicit, dual time-stepping method. The final algebraic system of equations is solved using a Conjugate Gradient method, in conjunction with Block Incomplete Lower-Upper factorisation. A number of turbulence models including one and two-equation statistical models as well as Large-Eddy Simulation (LES) and Detached Simulation (DES) formulations have been implemented into the code. At the moment, the classical Smagorinsky Sub-Grid Scale (SGS) model is used for LES whereas DES with both the one-equation Spalart-Allmaras and the two-equation $k-\omega$ and SST turbulence models have been integrated.

### Turbulence Modelling

The SST turbulence model was typically constructed as a 'blend' of the $k-\omega/k-\varepsilon$ models as mentioned by Menter[24] but are phrased in $k-\omega$ form in PMB. The blended values for the model coefficients $\alpha$, $\beta$, $\sigma_k^{-1}$ and $\sigma_\omega^{-1}$ are given by

$$B\begin{pmatrix} a \\ b \end{pmatrix} \equiv F_1 a + (1-F_1)\, b. \tag{1}$$

The blending function defined as

$$F_1 = \tanh\left(arg_1^4\right), \quad arg_1 = min\left[\max\left(\frac{k^{1/2}}{\beta^*\omega y}, \frac{500\nu}{y_n^2\omega}\right), \frac{2k\omega}{y_n^2 \max\left(\nabla k \cdot \nabla\omega, 0\right)}\right]. \tag{2}$$

The SST model places an additional vorticity-dependent limiter on the shear stress, which is denoted as $F_2$:

$$F_2 = \tanh\left(arg_2^2\right), \quad arg_2 = \max\left(\frac{2k^{1/2}}{\beta^*\omega y}, \frac{500\nu}{y^2\omega}\right). \tag{3}$$

### DES Formulation

Spalart[17] modified the one-equation Spalart-Allmaras model to achieve a DES equivalent. The only modification is in the dissipation term of the transport equation of $\tilde{\nu}$, given as

$$-C_{w1} f_{w1} \left(\frac{\tilde{\nu}}{\tilde{d}}\right)^2. \tag{4}$$

Originally,

$$\tilde{d} = d = \text{distance of the nearest wall} \tag{5}$$

whereas for DES, it is

$$\tilde{d} = C_{DES}\Delta \tag{6}$$

where $C_{DES}$ is the DES coefficient and $\Delta$ is the metric of the grid size.

In practice, the following is employed

$$\tilde{d} = \min\left(d, C_{DES}\Delta\right), \quad \Delta = \max\left(\Delta_x, \Delta_y, \Delta_z\right) \quad \forall \quad \text{cell}, \tag{7}$$

although other metric relations are also possible.

The concept of employing a DES-like approach for turbulence models other than the one-equation Spalart-Allmaras was originally proposed by Strelets[25] and later by Batten & Goldberg.[26] For the two-equation $k-\omega$ model, for instance, the only modification, as with the one-equation Spalart-Allmaras DES variant, is in the dissipation term

$$-\beta^* \rho \omega k \tag{8}$$

The turbulent length scale is defined by

$$l = \frac{k^{1/2}}{\beta^* \omega} \tag{9}$$

Re-arranging for $\beta^* \omega$ and substituting into equation 8 gives

$$-\rho \frac{k^{3/2}}{l} \tag{10}$$

where $l$ is given by

$$l = \min\left(l, C_{DES}\Delta\right). \tag{11}$$

$C_{DES}$ is set to 0.78 and $\Delta$ is as before.

## Description of Experiments

Wind tunnel experiments conducted by Ross[20] at Aircraft Research Association Ltd (ARA) at Bedford, UK, were used for validation. The ARA wind tunnel is a 9 by 8 foot continuous flow, transonic wind tunnel (TWT) with ventilated roof, floor and side walls. Results for the doors-on configuration are compared with the corresponding experimental data (comparisons being made at several locations along the cavity floor as illustrated in Figure 1). Where 2D cavity results are mentioned, the comparison was made with the 3D clean cavity experimental case, where the bay doors were open vertically at $90^o$ . The doors prevented any leakage at the cavity edges in the spanwise direction forcing the flow to channel into the cavity. In this configuration, the flow behaves as if it were 2D and is well represented by numerical modelling/simulation of a 2D cavity. Note that no experimental data was available for direct comparison with the numerical results obtained from the control study. Instead results were compared with experiment where no control device was used to illustrate the effectiveness of the control method.

The L/D=5 cavity model (with W/D=1) measured 20 inches in length, and 4 inches in width and depth. In the doors-on configuration, the doors were positioned at the front and rear walls in the z-direction and spanned the entire length of the cavity (see Figure 2(a)) and measured 0.375 inches width and 2 inches in height. The generic cavity rig model (designated as Model M219) was positioned at zero incidence and sideslip and the wind tunnel was operated at a Mach number of 0.85 and atmospheric pressure and temperature. Unsteady pressure measurements were registered inside and outside the cavity via Kulite pressure transducers: 10 pressure transducers were aligned along the centreline of the floor of the cavity rig, which was offset from the centreline of the actual cavity model (as shown in Figure 1), 2 on the flat plate ahead of the cavity, 1 on the flat plate aft of the cavity, 2 on the front and rear walls and 4 on the port side walls.[20] The data was sampled at 6000 Hz using a high-speed digital data acquisition system.

The measured data was presented in terms of Sound Pressure Level (SPL) and Power Spectral Density (PSD) plots. The SPLs are an indication of the intensity of noise generated inside the cavity and can be obtained from the measurements using the following equation:

$$\mathrm{SPL\,(dB)} = 20 \log_{10}\left(\frac{\mathrm{p_{rms}}}{2 \times 10^{-5}}\right) \tag{12}$$

where the $p_{rms}$ is the RMS pressure normalised by the International Standard for the minimum audible sound of $2 \times 10^{-5}$ Pa. Spectral analysis was performed using a Fast Fourier Transform (FFT) to obtain the power spectral density, which presents the RMS pressure versus frequency and is a measure of the frequency content inside the cavity.

Measurements of the cavity flow-field were provided by PIV experiments conducted by Ross[b]. A stereoscopic two-camera system was employed for velocity measurements accompanied with a two-head Nd-YaG laser. Each laser pulse was fired within time intervals of $1\mu$s. Four data acquisitions were taken with each

[b]Private communication.

acquisition comprising of 2 photographic images taken at 1$\mu$s intervals. The width of the laser sheet was limited to approximately 5.5 inches so the total cavity length of 20 inches was captured in 4 sections using motorised camera/laser traverse gear (Figure 2(b)). Seeding was provided by various combinations of water droplets sprayed in the settling chamber and vegetable oil mist diffusion from small holes in the cavity floor. Analysis of the data signals was performed by phase-locking onto each peak of signal and introducing a series of delays to synchronise image acquisitions at a particular part of the cycle. A number of acquisitions were then taken and averaged to define the flow-field at that part of the cycle. For highly unsteady flows with multiple cyclic components, it was recognised that phase-locking on any one component does not 'freeze' the flow-field. As highlighted by Ross[c], combined with the highly turbulent background, all aspects of a cavity flow are not likely to be accounted for. For a complete definition of the flow-field with time-dependency, very high-speed image acquisition equipment would be required.

## Results & Discussion

The paper is split up into three parts. The first section compares results between the URANS, LES and DES for the clean cavity with and without doors (Figures 3 to 6). The final part then analyses results from the control study where the effects of the spoiler, slanted cavity walls and steady jet blowing as a passive control device are investigated (Figures 9 to 15). No experimental data was available for direct comparison with the CFD results for the flow control study. Comparisons were made with the experimental data where no control device was used, to illustrate the effectiveness of the control method.

### Clean Cavity Flow Analysis

The grids used in the numerical modelling and simulation of the empty weapons bay modelled as a clean 3D, L/D=5, W/D=1 open rectangular cavity are described in Table 1. All dimensions in these grids were scaled with respect to the cavity length. For the DES and LES grids, the far-field length was set to 3.5 times the cavity length so as to minimise any spurious results from acoustic wave reflections. A flat plate 1.5 times the cavity length (as in the experiment) was used ahead of the cavity to allow the oncoming boundary layer to develop naturally.

*Doors-Off Results*

Results from the clean, doors-off cavity for the URANS, DES and LES methods are depicted in Figures 3 to 5, with unsteady pressure comparisons with experiment revealing best agreement with DES and LES (Figure 3(a)). URANS results were based on the coarse grid with Menter's Baseline $k-\omega$ model.[24] A time-step of 0.01 ($\equiv 1.814 \times 10^{-5}$s) was used for this computation — details of the grid are provided in Table 1. The fine grid was used for the DES computation with a time-step of 0.001 ($\equiv 1.814 \times 10^{-6}$s) and the very fine grid for the LES computation with the same time-step. The experimental signal was sampled at 6 kHz so the numerical results were sampled at the same rate for proper comparison.

The shape of the SPL curve for Menter's Baseline $k-\omega$ model still resembles the 'W' shape that is characteristic of the doors-on case, which will be discussed in greater detail in the following section (Figure 6(a)). Without doors, the flow inside and outside of the cavity is less constrained to move in the spanwise direction. The fact that Menter's Baseline $k-\omega$ model predicts a completely incorrect SPL shape (unlike LES and DES) suggests that it (and indeed URANS) has difficulty in accommodating effects of the greater transport and redistribution of energy and momentum in the spanwise direction. The difference in frequencies without the doors is clearly represented by the spectral analysis in Figure 3(b). The 3rd Rossiter mode ($\approx$ 600 Hz) is more dominant for the doors-off cavity case compared to the 2nd mode ($\approx$ 380 Hz) for the doors-on case. Although Menter's Baseline $k-\omega$ model predicts the 3rd mode relatively well, it fails to account for either the lower or higher frequencies. This is however not surprising since URANS can only account for the most energetic coherent structures in a flow. The 3rd Rossiter mode is the dominant frequency in the doors-off cavity configuration and so URANS captures this well but fails to account for any of the lower or higher frequencies.

Instantaneous Mach contours for both Menter's Baseline $k-\omega$ model and DES (with the one-equation Spalart-Allmaras model) along the cavity centreline are illustrated in Figure 4. The Mach number plots

[c]Private communication.

distinctly demarcate the lower-velocity regions (blue) inside the cavity from the transonic regions (yellow) outside the cavity. Where these two regions coalesce is where the shear layer is located. Menter's Baseline $k-\omega$ model always predicts a larger single primary vortex structure at the cavity rear with some combination of two or more counter-rotating vortices at the cavity front. The shear layer is also consistently found to span the cavity with distinct deflection at the cavity rear (Figure 4). It is this dual-vortex cycle inside the cavity that results in the 'W'-shaped SPL curve in Figure 3(a). The difference between the DES and URANS flow-field results lies in the behaviour of the shear layer and this is evident in Figure 4. At no point for the DES computations does the shear layer extend across the entire length of the cavity. At the most, the shear layer can be observed to be coherent up to the middle of the cavity at which point, if not earlier, it breaks down. What follows is intensive mixing and spreading of the energy from the shear layer and the free-stream with the lower-velocity flow region inside the cavity. The pressure at the cavity rear rises due to this mixing process and is manifested in the form of a rising SPL curve (Figure 3(a)).

With the shear layer detached, the flow within the cavity is no longer entrained within it and large vortical structures can no longer be sustained. More turbulence, higher frequencies and smaller vortices instead form. These interact with the cavity walls to create regions of higher pressure and more flow activity. Not confined by the shear layer, the flow can now be observed to 'spill' over the cavity in both the streamwise and spanwise directions. Indications of these 'spillages' can be distinctly seen in LES and, to a lesser extent, LES computations in Figure 5, which provides a three-dimensional perspective of the instantaneous flow field (using Mach contours normalised by the free-stream Mach number of 0.85) inside the 3D clean cavity in the doors-off case. As URANS does not predict the breakdown of the shear layer, these vortical 'spillages' are also not observed in URANS computations.

*Doors-On Results*

Figure 6 shows the difference between the DES, LES and URANS methods in the prediction of noise levels and frequencies for the clean, doors-on cavity configuration. The coarse grid was used with Menter's Baseline $k-\omega$ model for URANS computations with a time-step of 0.01 ($\equiv 1.814\times10^{-5}$s), the fine grid for the DES computation with a time-step of 0.001 ($\equiv 1.814\times10^{-6}$s) and the medium grid for the LES computation with a time-step of 0.005 ($\equiv 9.07\times10^{-6}$s). Due to the success of the DES with the one-equation Spalart-Allmaras turbulence model for the doors-off case, it was decided to run a fine grid computation using DES rather than using very fine grids with LES. Two sets of unsteady pressure experimental data were available for the doors-on case: one was sampled at 6 kHz and another with a higher sampling rate of 31.25 kHz. Both of these experimental data sets are included in Figure 6 to emphasise the importance of high resolution experimental data. All numerical results were sampled at 31.25 kHz.

Menter's Baseline $k-\omega$ turbulence model was used for URANS while the one-equation Spalart-Allmaras model was used with DES to realise the turbulent near-wall properties. Variations in SPLs across the cavity length along its floor is illustrated in Figure 6(a). All three methods agree reasonably well with experiment, with URANS agreeing even better with experiment in some cases. Near the front of the cavity, for instance, the shape of the SPL curve for Menter's Baseline $k-\omega$ model follows the experiment better than the DES and LES counterparts.

A closer inspection of the frequency content at the cavity rear ($x/L=0.95$) illustrates a less satisfactory agreement between Menter's Baseline $k-\omega$ model and experiment (Figure 6(b)). Neither the 1st ($\approx$ 160 Hz) nor the 3rd ($\approx$ 600 Hz) Rossiter modes are captured. The 2nd Rossiter mode ($\approx$ 400 Hz) is well captured but is over-predicted by about 1 kPa. This over-prediction was found to be a common occurrence for most URANS comparisons with experiment.

*PIV Comparisons*

PIV data was provided by Ross[d], as described above. The PIV experiment was conducted for the 3D cavity in the doors-on configuration only and so results from the corresponding doors-on computations are only compared with it.

Streamwise and transverse velocity profiles for three different stations inside the cavity (x/L=0.05, x/L=0.55 and x/L=0.95 - see Figure 1 for the positions of these pressure taps) for both DES and LES computations are illustrated in Figure 7. The black line denotes the PIV results. The three other plots included in the velocity profile plot correspond to the time-averaged DES results with the one-equation

[d]Private communication.

Spalart-Allmaras model (solid green line), DES results with the two-equation $k-\omega$ model (dashed red line) and LES results with the classical Smagorinsky sub-grid scale model (dashed-dot blue line) for the coarse grid (refer to Table 1 for information on the grids used) at a time-step of 0.01 ($\equiv 1.814\times10^{-5}$s). The results are encouragingly consistent for both DES variants and LES.

Agreement with PIV is, however, sensitive to the station analysed. At the first two stations, at x/L=0.05 (cavity front) and at x/L=0.55 (cavity middle), the agreement between DES, LES and PIV is good. At the cavity rear (x/L=0.95), agreement with PIV deteriorates. The explanation for this may lie in the manner in which the PIV experiment was conducted. As mentioned previously, the laser used for the PIV experiment had a width of approximately 5.5 inches, which is roughly equivalent to a quarter of the cavity length. The laser was fired at four different sections in order to cover the entire length of the cavity (Figure 2(b)). The resolution of the PIV experiment was found to be good at the first two stations that the computational results were analysed at, i.e. at x/L=0.05 and x/L=0.55, but was not at the third station, i.e. at x/L=0.95. This is illustrated in Figure 8, which indicates the variations in the streamwise and transverse velocity components along the length of the cavity for the PIV experiment at a distance equal to the depth of the cavity above the cavity lip. The experiment was conducted at a Mach number of 0.85 and a freestream velocity of 296 m/s. In sections 1 and 3 of the PIV experiment, which are where the first two stations x/L=0.05 and x/L=0.55 respectively lie, the laser resolution is good and the streamwise velocity is close to its anticipated value of 296 m/s (Figure 8(a)). In section 4, however, which is where the third station x/L=0.95 lies, the resolution deteriorates and the streamwise fluctuations are significantly larger. A consistent story is told by the transverse streamwise plots in Figure 8(b). This possibly explains the discrepancies between the LES, DES and PIV data at the cavity rear. This also further emphasises the problems with using PIV for highly unsteady flows at high Mach and Reynolds numbers. As mentioned by Ross[e], higher imaging and data acquisition equipment is likely to be required for consistently good resolution throughout the cavity cross-section.

## Cavity Flow Control

Effectiveness of the spoiler, slanted cavity walls and steady jet blowing as a passive control device were investigated in this study. For each control method, the control device was placed at different locations and its influence recorded. In each case, where no control method is used is denoted as 'baseline'. Although no experimental data was available for this control study, results were compared to the computational 'baseline' case as well as to the corresponding experimental results (i.e. for the clean, 2D, L/D=5 cavity where no control method was used) to illustrate effectiveness of the control method.

Due to the reasonable predictive capability of the SST turbulence model on coarse grids based on previous analyses and the requirement for low computational run-time, all computations performed in this control study used the SST model only. In this manner, turbulence modelling issues were minimised and any changes in the cavity flow can reasonably accurately be assumed to be predominantly dependant on the control method employed. Table 2 provides description of all the grids used for the control studies.

### *Spoiler*

The position of the spoiler relative to the cavity was varied and its effect on the cavity acoustics and flow structures studied. The width ($w_{sp}$) and height ($h_{sp}$) of the spoiler was kept fixed at 0.25 inches and 0.42 inches (which is approximately equal to the height of the boundary layer, $\delta$), respectively. Details of the grids used in this case are provided in Table 2. For clarity, the three different spoiler configurations are denoted as Cases 1, 2 and 3. Case 1 denotes the LE spoiler whose co-ordinates correspond to $x_{sp}/L=-0.2, y_{sp}/L=0$, Case 2 for the LE spoiler with co-ordinates $x_{sp}/L=-0.1, y_{sp}/L=0$ and Case 3 for the TE spoiler with co-ordinates $x_{sp}/L=1, y_{sp}/L=0$. A schematic of the different spoiler positions and appropriate dimensions is illustrated below in Figure 9(a).

Pressure traces for all the different spoiler positions at the cavity rear ($x/L=0.95$) along the cavity floor as well as SPLs are illustrated in Figure 10 below. Numerical and experimental results for the 'baseline' case (i.e. with no spoiler) are also indicated for reference.

Generally, the upstream spoiler produces less noise inside the cavity. For the LE spoiler located furthest upstream (Case 1), denoted by a red line with circular symbols, pressure amplitudes are completely damped out resulting in a drop in the SPLs by as much as 30 dB from experiment. This results in a flat SPL curve

[e]Private communication.

(Figure 10(b)) and is indicative of frequencies being damped out. As the spoiler is moved closer to the front corner (Case 2a), more noise is generated at the cavity rear ($x/L = 0.95$) as is indicated by the peaks in the SPL curve at about $x/L = 0.15$ and $x/L = 0.9$, respectively. Variations in the pressure signal are therefore greater at these locations as the spoiler is moved closer to the front. These fluctuations are however much smaller than the experimental pressure oscillations and so the pressure signal appears flat for the scale drawn in Figure 10(a). Noise levels are consequently slightly higher for this case relative to the spoiler furthest upstream (Case 1) by about 5 dB but this is still about 25 dB lower than experiment at the cavity rear ($x/L = 0.95$).

When the spoiler is placed at the downstream cavity corner (Case 3), pressure amplitudes increase more significantly resulting in an increase in the overall noise levels generated at the cavity floor by as much as 6-7 dB at the cavity rear (Figure 10(b)). Wavelengths of the pressure oscillations (denoted by magenta lines with square symbols) for the trailing-edge spoiler are found to be greater than compared to experiment and suggests that lower frequencies are more dominant. This dramatic change in the periods of the frequencies appears to suggest that the wake mode has been activated as was encountered in previous computations.

Illustration of the flow-field inside the cavity with the spoiler is shown in Figure 11, which displays time-averaged plots with Mach contours and streamlines. For reference, flow-field inside the cavity without a spoiler is also included (Figure 11(a)). Analysis of the flow-field plots for the LE spoilers (Cases 1 and 2a) clearly indicate that the spoiler forces the flow to separate ahead of the normal separation point at the cavity lip (see Figure 11(a)), deflecting the flow upwards. Momentum of the free-stream then 'carries' this prematurely-separated flow further downstream. Although a shear layer still forms across the cavity opening, it is now shifted upwards and the flow re-enters the cavity tangentially to the downstream wall, i.e. flow enters vertically from the transverse direction (Figures 11(b) and 11(c)). Flow is therefore observed to graze along the downstream wall rather than impinge against it. In contrast, the shear layer approaches the cavity rear for the baseline case in the streamwise direction and therefore impacts the downstream wall almost perpendicularly (Figure 11(a)). The mass breathing process that would normally initiate injection and ejection of fluid in and out of the cavity due to the deflection of the shear layer is thus eliminated and generation of acoustical disturbances (and subsequent propagation of acoustic waves) minimised. In this manner, higher frequencies are also eliminated.

By changing the position of the spoiler from upstream to downstream of the cavity, the physics of the flowfield inside the cavity changes completely. For the trailing-edge spoiler, the shear layer mode no longer exists as it does for the case without the spoiler (Figure 11(a)). Instead, vortex shedding occurs at the cavity lip and the flow switches to the wake mode (Figure 11(d)). It was found that the trailing-edge spoiler decelerates a larger proportion of the oncoming free-stream air thereby creating a region of very high pressure at the cavity rear. Near the cavity front, the flow separates at the cavity lip and rolls into the cavity. The high pressure region at the cavity rear, however, prevents the vortex from convecting any further downstream. As a result, the vortex is forced to expand outwards of the cavity. This large vortex forces more flow to deflect around it and moves the separation point ahead of the cavity further upstream. This results in another vortex that rolls into the cavity and a continuous vortex-shedding cycle that generates the large pressure oscillations inside the cavity as illustrated in Figure 10. Large peripheral velocities of the vortices (depicted by the lighter, higher Mach regions in Figure 11(d)) near the cavity floor are responsible for more intense shearing of the vortex with the walls and hence causes noise levels much higher than experiment and even the baseline case (Figure 10(b)).

*Slanted Cavity Walls*

For the slanted cavity walls, the different slopes investigated are illustrated in the schematic in Figure 9(b). Details of the grids used for each of these cases are provided in Table 2. Three different scenarios were investigated: slanting the front cavity wall only, slanting the rear cavity wall only and slanting both front and rear walls. The angle of slant was kept fixed at 45° in all these cases.

Figure 12 below plots the SPLs and pressure traces (at $x/L = 0.95$) for a slanted front wall (red with circular symbols), slanted rear wall (green with crosses) and both walls slanted (magenta with square symbols). Experimental (black with diamond symbols) and numerical (blue with plus signs) results corresponding to the baseline case where no slant was implemented are also included for demonstration of the effectiveness of the control method.

As far as mitigating the intensity of noise is concerned, slanted walls, irrespective of position, appear to be an effective method with maximum pressure amplitudes generally tending to be lower than those

given by experiment or numerically for the baseline case. Slanting only the front wall however appears to be the least effective of all the three cases investigated with noise levels significantly higher at around the x/L=0.25 and x/L=0.75 positions. The 'dips' in the SPL curve, which are approximately coincident to the average locations of the cores of the vortices, are also damped out (Figure 12(b)). Slanting the downstream wall produces greater reductions in SPLs throughout the cavity length (by $\approx$ 5-12 dB). Slanting both front and rear walls appears to be quieter at the rear ($x/L = 0.95$) while the rest of the noise level distribution (especially along the cavity middle section) resembles the slanted front wall only results.

Illustrations of the time-averaged flow-field inside the cavity for different slanted wall configurations are provided in Figure 13 below. Plots contain streamlines superimposed on Mach contours normalised with respect to the free-stream Mach number, $M_\infty = 0.85$. Boundaries and thicknesses of the shear and boundary layers are clearly defined in this manner as is the degree of flow intensity inside the cavity. For reference, the flow-field with no walls slanted is also included (Figure 13(a)). Irrespective of which wall is slanted, the front wall corner vortex has largely disappeared. The high Mach region along the cavity floor (distinctly evident from the lighter, green Mach contours) extends across a greater proportion of the cavity length. Noise generated on the cavity floor is therefore more distributed. Overall noise levels are however only significantly lower when the rear wall is slanted (Figure 13(c)). When the front wall is slanted (Figure 13(b)), SPLs are still of the same magnitude as that of experiment and the numerical results with no slant used (Figure 12(b)). This suggests that moving the position of the front corner further upstream (while keeping the L/D ratio of the cavity fixed) can cause adverse effects. Changing the angle of both walls merely combines the adverse effects of slanting the front wall and the positive effects of slanting the rear wall to give a compromised solution (Figure 13(d)).

The downstream corner is also naturally located further downstream as a consequence of slanting the cavity back wall. This forces the shear layer and any flow structures created to remain almost completely entrained within the cavity and thus the mass breathing process is minimised. Furthermore, with the rear wall slanted at 45$^o$ , the geometrical surface area of the downstream wall has increased by a factor of $\sqrt{2}$. Stress generated by the shearing of the vortex with the walls is therefore more distributed. Consequently, the noise levels generated at the cavity rear are much lower (by $\approx$ 7 dB) compared to experiment (see Figure 12(b)). Containment of the flow within the confinements of the cavity walls makes the flow intrinsically less unsteady. Vortical movement and shear layer deflection is minimised as a result. When both the front and rear walls are slanted, flow features are an amalgamation of the individually slanted front and rear walls. At the front, the streamwise velocity trace is therefore similar to the slanted front wall only and at the cavity rear it resembles the slanted rear wall only results.

*Steady Jet Blowing*

The final control method analysed here involves steady jet blowing, which endeavours to influence the flow in the cavity by blowing additional air into it. The basic concept of the steady jet is taken from Lamp & Chokani[27] where the jet exit velocity is calculated based on a reservoir total pressure and total temperature, assuming isentropic conditions. The angle of the jet here has been fixed to be perpendicular to the flow. For each case presented, the jet exit Mach number is set to $0.1M_\infty$. With a total reservoir pressure and temperature of 2 atmospheres and 298 K respectively, the jet exit velocity was calculated to be 29.4 m/s. The jet slot width, $w_j$, was also kept fixed at 0.02L. For this case, the blowing co-efficient, $C_\mu$, derived as the ratio of the exit jet to the free-stream mass flow rate, comes to 0.005. With these jet configurations, computations with three different jet locations were conducted: upstream (i.e. jet located ahead of cavity front corner [$x_j/L = -0.02$,$y_j/L = 0$]), front wall (i.e. jet located at [$x_j/L = 0$,$y_j/L = -0.02$]) and rear wall (i.e. jet located at [$x_j/L = 1$,$y_j/L = -0.02$]). A schematic of the different jet positions is depicted in Figure 9(c).

In all jet locations, pressure oscillations and frequencies experienced in the baseline case were damped out with steady jet blowing and the flow became steady. This is illustrated in Figure 14, which shows the SPLs and pressure traces for the jet located upstream (red line with circular symbols), jet located at the front cavity wall (green line with crosses) and jet located at the downstream cavity wall (magenta line with square signs). For reference, experimental (black line with diamond symbols) and numerical (blue with plus signs) results corresponding to the baseline case without any jet are also included.

The reason why the jet is so effective in controlling the self-sustained oscillations inside the cavity can be illustrated using the time-averaged Mach contour plots in Figure 15. With the jet located at the front wall 15(c), the jet simply adds more momentum to the shear layer. The extra momentum ensures that the shear

layer entirely bridges the cavity opening and minimises the extent to which energy is transferred from the shear layer to within the cavity. Acoustical disturbances caused by the impingement of the flow at the cavity downstream wall are therefore eliminated. Consequently, the pressure waves and hence the self-sustained pressure oscillations that drive the flow cycle are cancelled out. The flow becomes steady and the typical dual-vortex cycle with large shear layer deflection as observed in the baseline case (Figure 15(a)) becomes a single, static vortex with no shear layer deflection with steady jet blowing (Figure 15(c)).

In contrast, the rear wall jet extracts momentum from the shear layer causing it to decelerate and diffuse. This diffused shear layer is clearly evident from the larger cross-sectional area of the flow shed downstream of the cavity in Figure 15(d). Comparisons of SPLS between the front wall and rear wall jet reveals that the rear wall jet produces significantly more noise. The greater region of higher Mach numbers depicted by the lighter, green colours in Figure 15(d) is indicative of the greater shear between the vortices and the cavity floor and hence greater noise.

For the upstream jet, where the jet is fired vertically upwards, momentum is added to the transverse component rather than the streamwise component as was the case with the front wall jet. Shear layer is therefore forced to detach further upstream of the cavity and its curved trajectory creates a more favourable pressure gradient that accelerates the flow over it (Figure 15(b)). With the shear layer inclined at an angle and having more energy, it redistributes its momentum into the cavity. Vortices of larger circulation strength are therefore created as depicted by the region of stronger Mach number at the rear of the cavity floor in Figure 15(b) compared to other jet locations. Higher peripheral vortex velocities at the cavity floor therefore lead to the higher noise levels inside the cavity for the upstream jet (Figure 14(b)). As the shear layer is redirected by the upstream jet, impingement of the shear layer with the cavity rear wall is again negated and the self-sustained pressure oscillations are attenuated. The result is therefore a steady solution (Figure 14(a)) and a single-vortex structure presides inside the cavity (Figure 15(b)).

## Conclusions

Analysis and control of weapon bays modelled by a 3D cavity with L/D=5 and W/D=1 are presented. All computations with a free-stream Mach of 0.85 and a Reynolds number of 6.783 million using the PMB code developed by University of Glasgow. Analysis of clean weapon bays are first presented where results from URANS, LES and DES are compared. Control of clean weapon bays is then demonstrated using passive control methods and the paper is concluded with an illustration of the preliminary results obtained with a store housed inside the cavity.

Analysis of unsteady pressure measurements with experiment revealed that both DES and LES consistently gave better agreement than URANS in terms of both frequency content, phase and noise levels for both the doors-on and doors-off configurations. Menter's Baseline $k-\omega$ model was also run for this 3D cavity with and without doors but had difficulty in capturing most of the higher (and in some cases, some of the lower) frequencies in both cases. For the doors-off case, Menter's Baseline $k-\omega$ model still predicted a 'W'-shaped SPL curve as it did for the doors-on case unlike LES and DES, which correctly predicted the 'tick'-shape. Flow-field visualisation for the doors-off cavity with Menter's Baseline $k-\omega$ model and DES revealed that DES predicted a breakdown of the shear layer while Menter's baseline $k-\omega$ model consistently illustrated a coherent shear layer that spanned the cavity. It was concluded that URANS had difficulty in accounting for the larger transport and/or diffusion of energy and momentum present in the doors-off case.

Streamwise and transverse velocity plots were compared for the doors-on case with PIV measurements and showed consistently good agreement at the cavity front and middle for different DES variants and LES. At the cavity rear, the agreement with PIV deteriorated and these discrepancies may be attributed to poor resolution in the PIV experiment at this position.

Calculations with different passive control methods with the 2D, L/D=5 cavity were conducted in the aim of reducing the high noise levels and large frequency content observed inside the cavity. Effectiveness of the spoiler, slanted cavity walls and steady jet blowing as a passive control method was investigated. For the spoiler, reductions in SPLs of about 30 dB were achieved when the spoiler was placed upstream of the cavity but overall noise levels increased when the spoiler is placed aft of the cavity. With slanted cavity walls, slanting the front wall induced massive separation at the front corner and maintained relatively high noise levels inside the cavity. When the rear wall is cavity flow environment is improved and a noise level reduction of about 10 dB can be achieved. Steady jet blowing was found to be the most effective of all passive control methods. Although jets fired from different positions all completely suppressed all acoustic tones making

the flow steady, the front wall jet proved to be the most effective obtaining noise level reductions of up to 35 dB.

## Acknowledgements

The work detailed in this paper was supported by both BAE Systems and the Engineering and Physical Sciences Research Council (EPSRC). The authors would like to extend their gratitude to Drs. John Ross and Graham Foster of QinetiQ (Bedford) for providing the experimental data.

## References

[1]Rossiter, J., "Wind Tunnel Experiments on the Flow Over Rectangular Cavities at Subsonic and Transonic Speeds," Tech. Rep. 64037, Royal Aircraft Establishment, October 1964.

[2]D. Rockwell and E.Naudascher, "Review— Self-Sustaining Oscillations of Flow Past Cavities," Vol. 100, No. 2, June 1978, pp. 152–165.

[3]C.K.W. Tam and P.J.W. Block, "On the Tones and Pressure Oscillations Induced by Flow Over Rectangular Cavities," *Journal of Fluid Mechanics*, Vol. 89, No. 2, 1978, pp. 373–399.

[4]M.B. Tracy, E.B. Plentovich and J. Chu, "Measurements of Fluctuating Pressure in a Rectangular Cavity in Transonic Flow at High Reynolds Numbers," Technical Memorandum 4363, June 1992.

[5]Heller, H. and Delfs, J., "Cavity Pressure Oscillations: The Generating Mechanism Visualized," *AIAA*, Vol. 33, No. 8, August 1995, pp. 1404–1411.

[6]S.A. Ritchie, N.J. Lawson and K. Knowles, "An Experimental and Numerical Investigation of an Open Transonic Cavity," *21st Applied Aerodynamics Conference*, AIAA, Orlando, Florida, June 2003.

[7]M.J. Esteve, P. Reulet and Millan, P., "Flow Field Characterisation within a Rectangular Cavity," *10th International Symposium Applications of Laser Techniques to Fluid Mechanics*, July 2000.

[8]O. Baysal, S. Srinivasan and R.L. Stallings Jr., "Unsteady Viscous Calculations of Supersonic Flows Past Deep and Shallow Three-Dimensional Cavities," *AIAA 26th Aerospace Sciences Meeting*, AIAA, Reno, Nevada, January 1988, AIAA Paper 88-0101.

[9]Orkwis, P. and Disimile, P., "Transient Shear Layer Dynamics of Two- and Three-Dimensional Open Cavities," Tech. Rep. ADA 298030, Air Force Office of Scientific Research, 1995.

[10]Jeng, Y. and Payne, U., "Numerical Study of a Supersonic Open Cavity Flow and Pressure Oscillation Control," *AIAA*, Vol. 32, No. 2, March-April 1995, pp. 363–369.

[11]Chung-Jen Tam, P.D. Orkwis and P.J. Disimile, "Algebraic Turbulence Model Simulations of Supersonic Open-Cavity Flow Physics," *AIAA*, Vol. 34, No. 11, November 1996, pp. 2255–2260.

[12]Shieh, C. and Morris, P., "Comparison of Two- and Three-Dimensional Turbulent Cavity Flows," *39th AIAA Aerospace Sciences*, AIAA, January 2001, AIAA Paper 2001-0511.

[13]D. Lawrie, *Investigation of Cavity Flows at Low and High Reynolds Numbers Using Computational Fluid Dynamics*, Ph.D. thesis, University of Glasgow, University of Glasgow, Glasgow, 2004.

[14]Rizzetta, D. and Visbal, M., "Large-Eddy Simulation of Supersonic Cavity Flowfields Including Flow Control," *32nd AIAA Fluid Dynamics Conference*, AIAA, 2002, AIAA Paper 2003-0778.

[15]L. Larchevêque, P. Sagaut and T-H Lê, "Large-Eddy Simulation of Flows in Weapon Bays," *41st AIAA Aerospace Sciences Meeting and Exhibit*, AIAA, 2003, AIAA Paper 2003-0778.

[16]B.R. Smith, T.J. Welterlen and N.D. Domel, "Large Eddy-Simulation for the Analysis of Weapon Bays Flows," Tech. rep., Lockheed Martin Aeronautics Company, June 2001.

[17]Spalart, P., "Strategies for Turbulence Modelling and Simulations," *International Journal of Heat and Fluid Flow*, Vol. 21, February 2000, pp. 252–263.

[18]A. Hamed, D. B. and K.Das, "Detached Eddy Simulations of Supersonic Flow over Cavity," *Unknown*, AIAA, 2003, AIAA Paper 2003-0549.

[19]Vishwanathan, A. and Squires, K., "Detached Eddy Simulation of the Flow over an Axisymmetric Cavity," *Aerospace Sciences Meeting 2003*, AIAA, January 2003, AIAA Paper 2003-0265.

[20]Ross, J., "Cavity Acoustic Measurements at High Speeds," Tech. Rep. DERA/MSS/MSFC2/TR000173, QinetiQ, March 2000.

[21]Ross, J. and Peto, J., "The Effect of Cavity Shaping, Front Spoilers and Ceiling Bleed on Loads Acting on Stores, and on the Unsteady Environment Within Weapon Bays," Tech. rep., QinetiQ, March 1997.

[22]L.N. Cattafesta, D. Williams, C. Rowley and F. Alvi, "Review of Active Control of Flow-Induced Cavity Resonance," *33rd AIAA Fluid Dynamics Conference*, AIAA, June 2003, AIAA Paper 2003-3567.

[23]K.J. Badcock, B.E. Richards and M.A. Woodgate, "Elements of Computational Fluid Dynamics on Block Structured Grids Using Implicit Solvers," *Progress in Aerospace Sciences*, Vol. 36, 2000, pp. 351–392.

[24]Menter, F., "Two-Equation Eddy-Viscosity Turbulence Models for Engineering Applications," *AIAA*, Vol. 32, No. 8, August 1994, pp. 1598–1605.

[25]Strelets, M., "Detached Eddy Simulation of Massively Separated Flows," *39th AIAA Aerospace Sciences Meeting*, AIAA, January 2001, AIAA Paper 2001-0879.

[26]P. Batten, U. Goldberg and S. Chakravarthy, "Sub-Grid Turbulence Modeling for Unsteady Flow with Acoustic Resonance," *38th AIAA Aerospace Sciences*, AIAA, January 2000, AIAA Paper 00-0473.

[27]Lamp, A. and Chokani, N., "Computation of Cavity Flows with Suppression Using Jet Blowing," Vol. 34, No. 4, July-August 1997, pp. 545–551.

**Table 1. Information on grids used for both the clean cavity in the doors-off and the doors-on at 90° configurations.**

| Grid Type | Pts. in Cavity (Overall) | Wall-Spacing | Blocks in cavity (Overall) |
|---|---|---|---|
| **Clean cavity with doors-on (at 90° )** | | | |
| **2D URANS (Coarse)** | 10,302 (33,250) | $1.05 \times 10^{-5}$ | 1 (6) |
| **3D URANS** | 446,824 (1,483,173) | $1 \times 10^{-5}$ | 20 (110) |
| **3D LES/DES (Coarse)** | 179,520 (1,248,544) | $3.125 \times 10^{-3}$ | 64 (240) |
| **3D LES/DES (Medium)** | 493,679 (2,218,854) | $3.125 \times 10^{-3}$ | 64 (240) |
| **3D LES/DES (Fine)** | 1,177,646 (4,783,162) | $7.1825 \times 10^{-4}$ | 64 (240) |
| **Clean cavity with doors-off** | | | |
| **3D URANS** | 305,424 (1,174,824) | $2.214 \times 10^{-5}$ | 20 (110) |
| **3D LES/DES (Coarse)** | 179,520 (1,225,824) | $3.125 \times 10^{-3}$ | 64 (256) |
| **3D LES/DES (Medium)** | 493,679 (2,178,480) | $3.125 \times 10^{-3}$ | 64 (256) |
| **3D LES/DES (Fine)** | 1,177,646 (4,696,128) | $7.1825 \times 10^{-4}$ | 64 (256) |
| **3D LES/DES (Very Fine)** | 2,097,152 (8,388,608) | $5 \times 10^{-5}$ | 64 (256) |

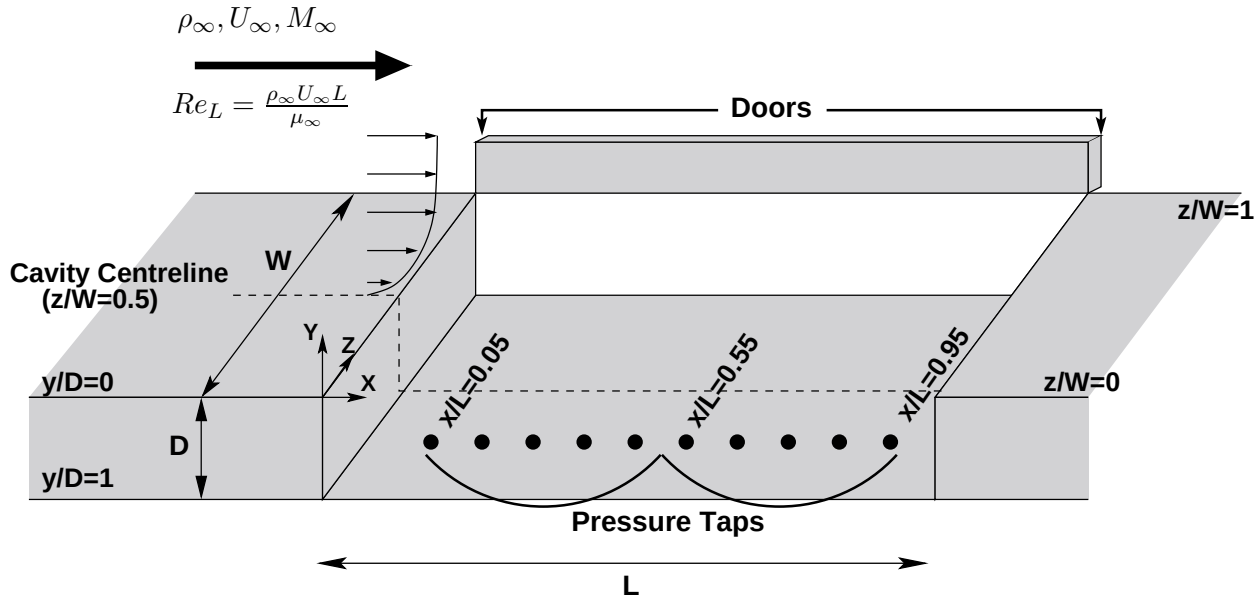


**Figure 1. Schematic describing cavity geometry and notation used. The ten pressure taps denoted by black dots correspond to the experimental pressure locations and represent where the SPL and PSD data was calculated and compared, i.e. at z/W=0.25 and along the cavity floor (y/D=1).**

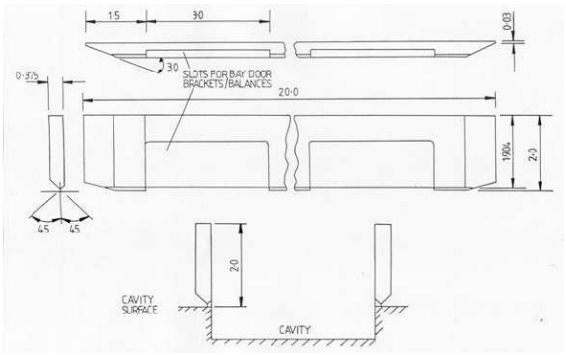


(a) Cavity Geometry

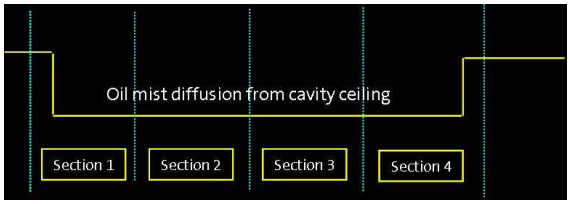


(b) PIV Experiment

**Figure 2. Schematic of the wind tunnel cavity geometry (including the doors-on configuration) on the left and an illustration of the 4 different sections along cavity for which laser data acquisitions were taken with the PIV experiment on the right.**

**Table 2. Information about the grids used for the 2D, L/D=5, clean cavity control study.**

| Grid Type | Pts. in Cavity (Overall) | Wall-Spacing | Blocks in cavity (Overall) |
|---|---|---|---|
| **2D L/D=5 clean cavity** | | | |
| **Coarse** | 10,302 (33,250) | $1.05 \times 10^{-5}$ | 1 (6) |
| **2D L/D=5 cavity with spoiler** | | | |
| **LE Spoiler (Case 1)** | 10,200 (80,658) | $5 \times 10^{-6}$ | 2 (17) |
| **LE Spoiler (Case 2)** | 22,800 (150,450) | $5 \times 10^{-6}$ | 2 (17) |
| **TE Spoiler (Case 3)** | 10,200 (65,860) | $5 \times 10^{-6}$ | 2 (15) |
| **2D L/D=5 cavity with slanted walls ($\theta = 45^{o}$ )** | | | |
| **Slanted Front Wall** | 11,016 (35,394) | $5 \times 10^{-6}$ | 2 (8) |
| **Slanted Rear Wall** | 9,894 (31,212) | $5 \times 10^{-5}$ | 2 (8) |
| **Slanted Front & Rear Walls** | 10,302 (31,926) | $7 \times 10^{-5}$ | 1 (6) |
| **2D L/D=5 cavity with steady jet blowing ($M_j = 0.1M_\infty$)** | | | |
| **Front Wall Jet** | 25,654 (46,972) | $5 \times 10^{-6}$ | 4 (9) |
| **Rear Wall Jet** | 25,856 (47,174) | $5 \times 10^{-6}$ | 4 (9) |
| **Upstream Jet** | 30,408 (103,178) | $5 \times 10^{-6}$ | 6 (24) |

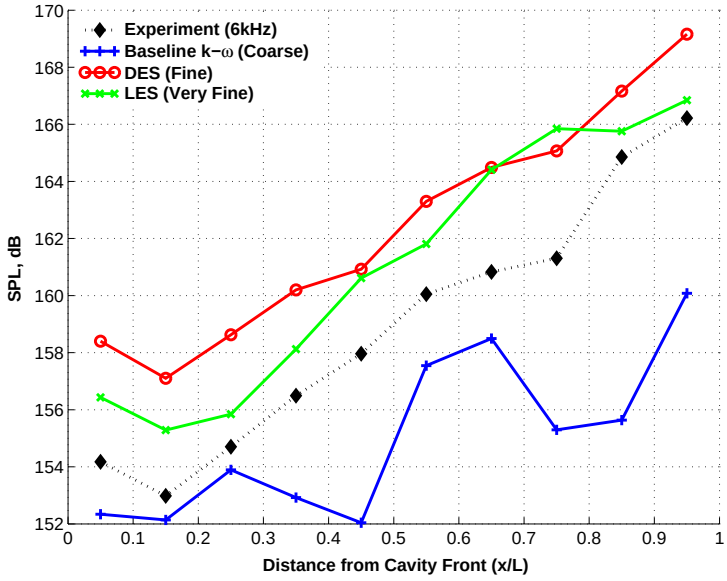


(a) SPLs

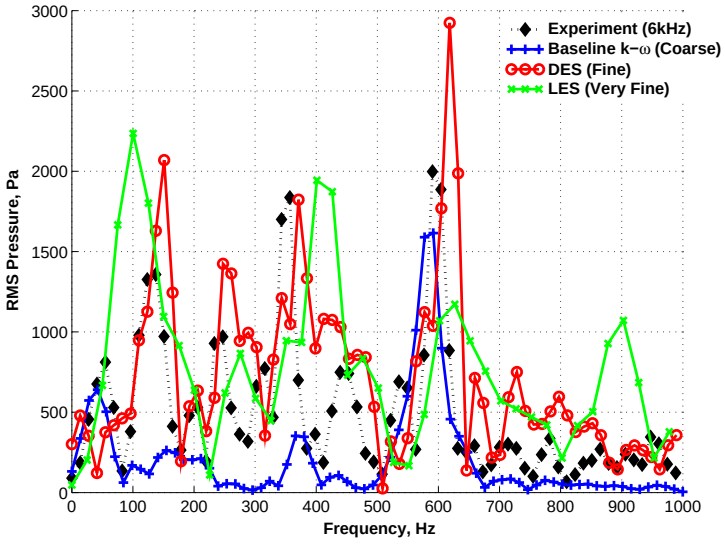


(b) PSD ($x/L = 0.95$)

**Figure 3. SPL and PSD plots (at $x/L = 0.95$) for the 3D, L/D=5, W/D=1, clean cavity with doors-off using the coarse grid for URANS (with Menter's Baseline $k-\omega$ model), fine grid for DES (with Spalart-Allmaras model) and very fine grid for LES (with Smagorinsky SGS). Plots taken at z/W=0.25 and along the cavity floor (y/D=1).**

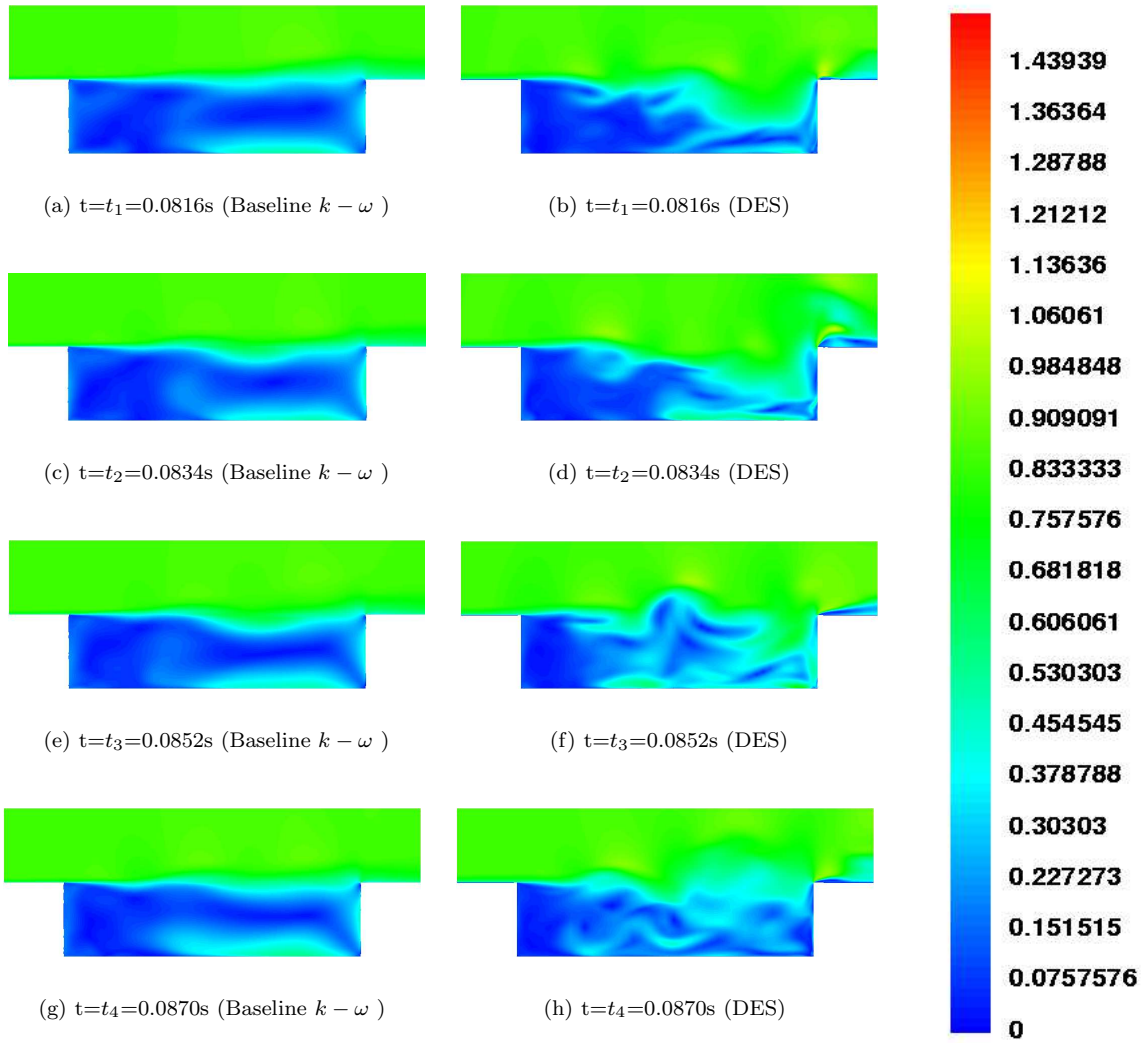


(a) t=$t_1$=0.0816s (Baseline $k-\omega$ )

(b) t=$t_1$=0.0816s (DES)

(c) t=$t_2$=0.0834s (Baseline $k-\omega$ )

(d) t=$t_2$=0.0834s (DES)

(e) t=$t_3$=0.0852s (Baseline $k-\omega$ )

(f) t=$t_3$=0.0852s (DES)

(g) t=$t_4$=0.0870s (Baseline $k-\omega$ )

(h) t=$t_4$=0.0870s (DES)

**Figure 4. Instantaneous Mach contours with streamlines for the clean cavity with no-doors illustrating flow features inside the 3D cavity at for 4 different time-steps during flow cycle for the coarse URANS (Menter's Baseline $k-\omega$ turbulence model) and fine DES (one-equation Spalart-Allmaras turbulence model) computations. Plots taken along the cavity centreline (z/W = 0.5).**

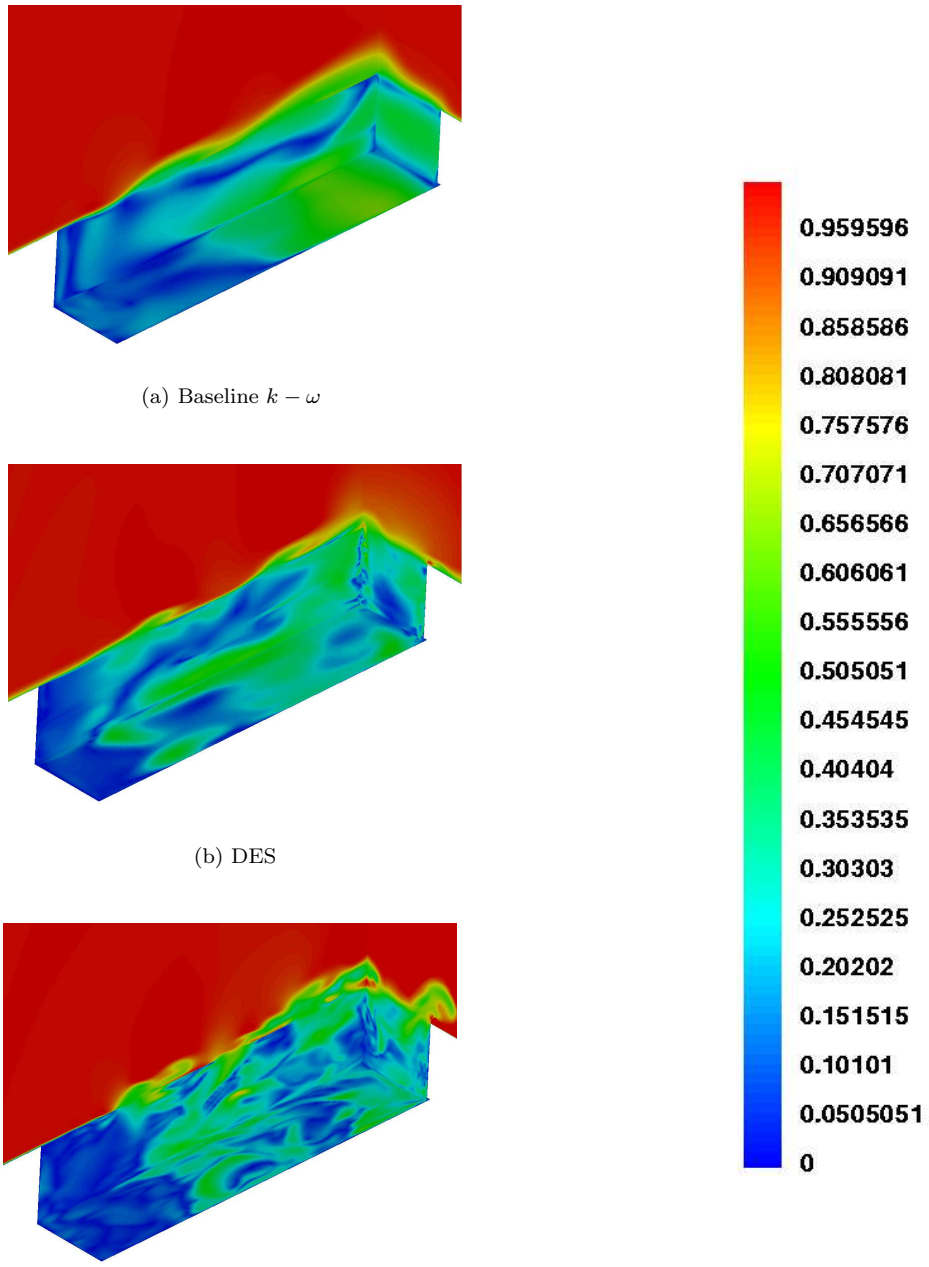


(a) Baseline $k-\omega$

(b) DES

(c) LES

**Figure 5. Three-dimensional perspective of the flow field inside the 3D L/D=5 clean cavity with doors-off for the URANS (with the Menter's Baseline $k-\omega$ model), DES (with the one-equation Spalart-Allmaras model) and LES (with the classical Smagorinsky SGS) methods. Plots show instantaneous Mach contours normalised by the free-stream Mach number of 0.85.**

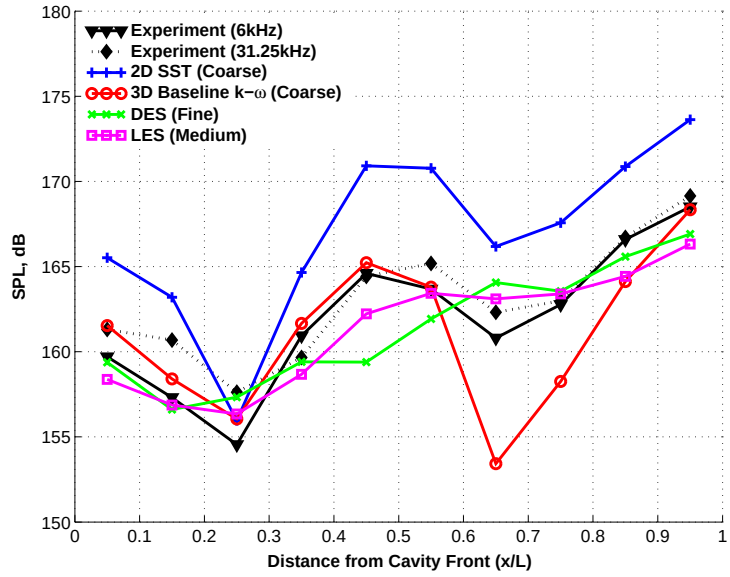


(a) SPLs

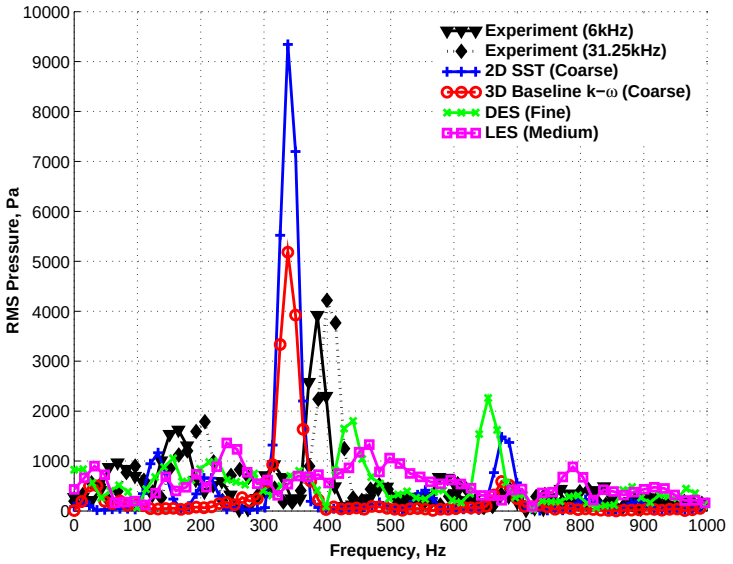


(b) PSD ($x/L = 0.95$)

**Figure 6. SPL and PSD plots (at $x/L = 0.95$) for the L/D=5, W/D=1, clean cavity with doors-on at 90° vertically with the 2D coarse URANS grid (with Menter's SST turbulence model), 3D URANS grid (with Menter's Baseline $k - \omega$ model), fine DES grid (Spalart-Allmaras model) and medium LES grid (Smagorinsky SGS). Plots taken at z/W=0.25 (for 3D results) and along the cavity floor (y/D=1). Experimental results with 6kHz and 31.25 kHz sampling rates included.**

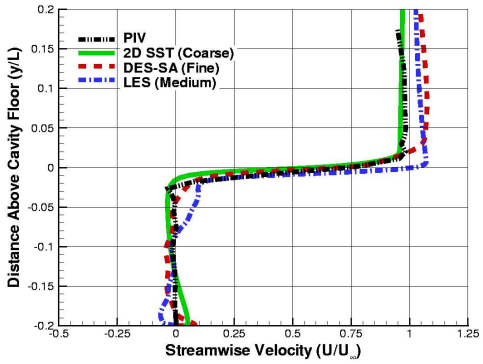


(a) U-Velocity (x/L=0.05)

Profile located within Section 1 of Figure 2(b)

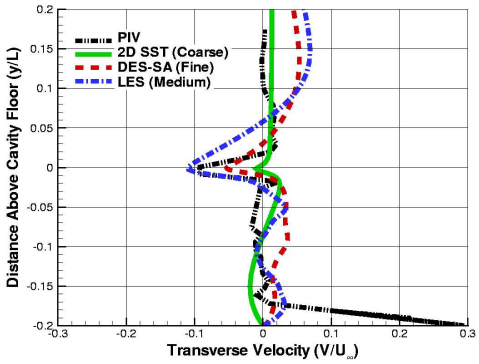


(b) V-Velocity (x/L=0.05)

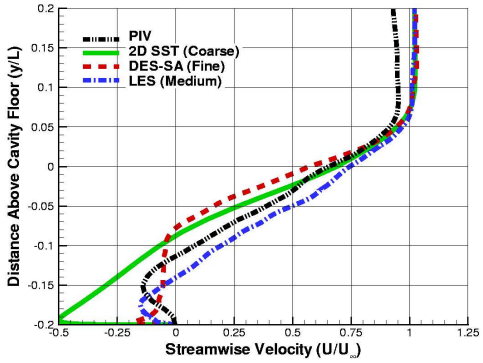


(c) U-Velocity (x/L=0.55)

Profile located within Section 3 of Figure 2(b)

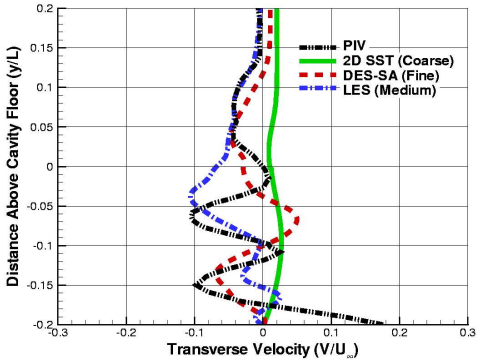


(d) V-Velocity (x/L=0.55)

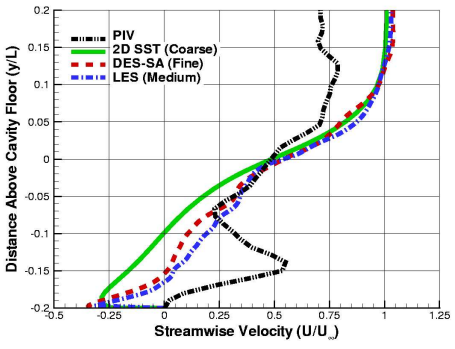


(e) U-Velocity (x/L=0.95)

Profile located within Section 4 of Figure 2(b)

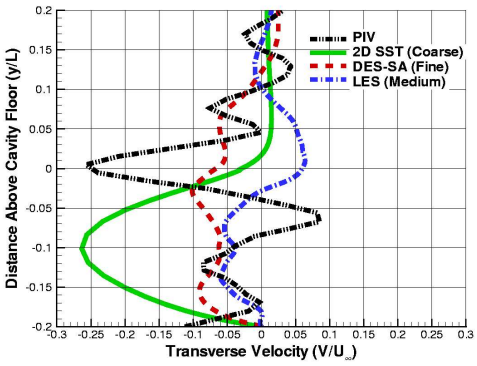


(f) V-Velocity (x/L=0.95)

**Figure 7. Time-averaged streamwise ($\frac{U}{U_\infty}$) & transverse ($\frac{V}{V_\infty}$) velocity profiles for the clean cavity with doors-on at 3 locations along cavity floor at x/L=0.05, x/L=0.55 and x/L=0.95. Results from coarse grid with time-step of 0.01 ($\equiv 1.814 \times 10^{-5}$s) used for 2D URANS, fine grid with time-step of 0.01 ($\equiv 1.814 \times 10^{-6}$s) used for DES-SA and medium grid with time-step of 0.005 ($\equiv 9.07 \times 10^{-6}$s) for LES. PIV data denoted by black line.**

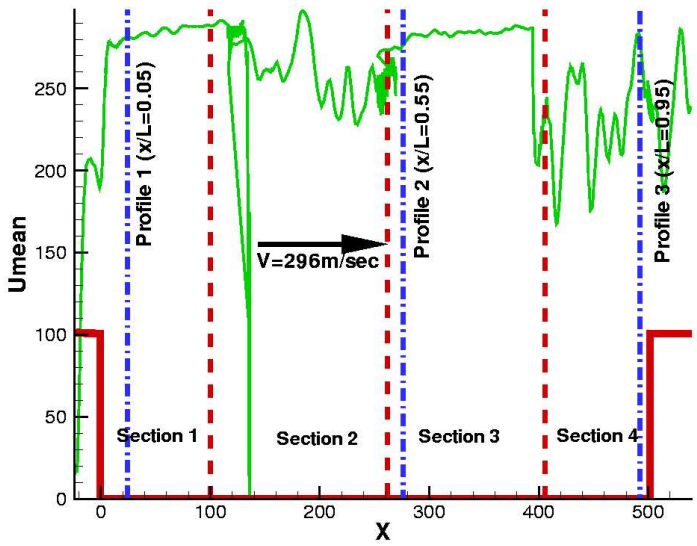


(a) PIV Streamwise (U) Velocity

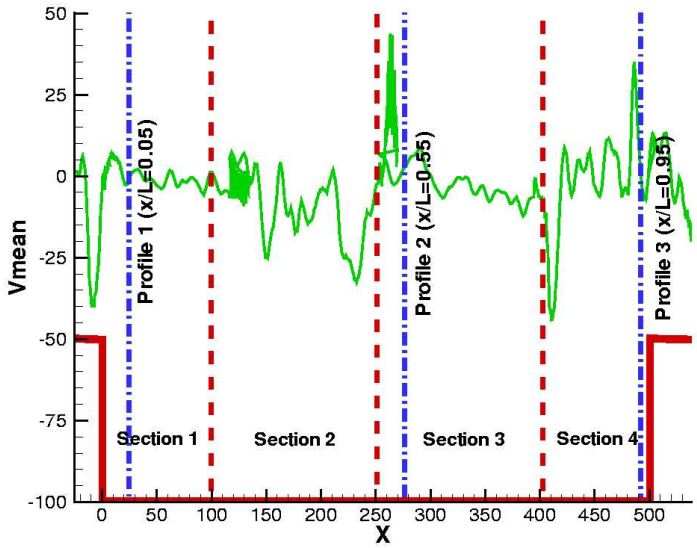


(b) PIV Transverse (V) Velocity

**Figure 8. Streamwise & transverse velocity traces at a distance equal to the depth of the cavity above the cavity lip. At cavity front and middle, PIV resolution is good and the free-stream velocity is as it should be, i.e. 296 m/s. Near cavity rear PIV reslution becomes poor: free-stream velocity is no longer equal to 296 m/s and fluctuates severely - transverse velocity plot indicates the same. As a result, comparisons with CFD are poorest when comparing with PIV data at the cavity rear (e.g. at x/L=0.95).**

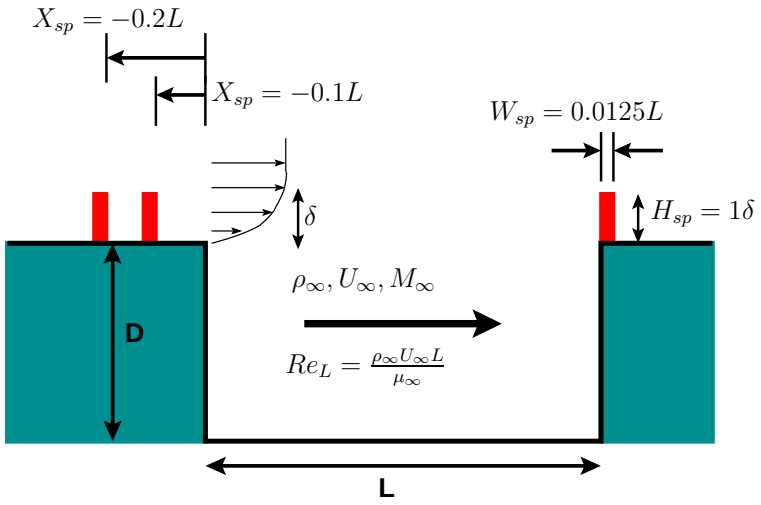


(a) Spoiler

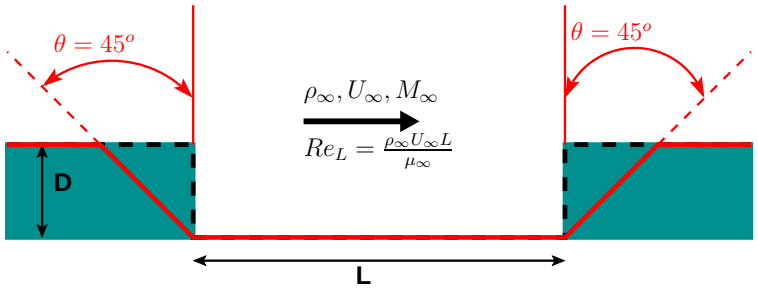


(b) Slanted Walls

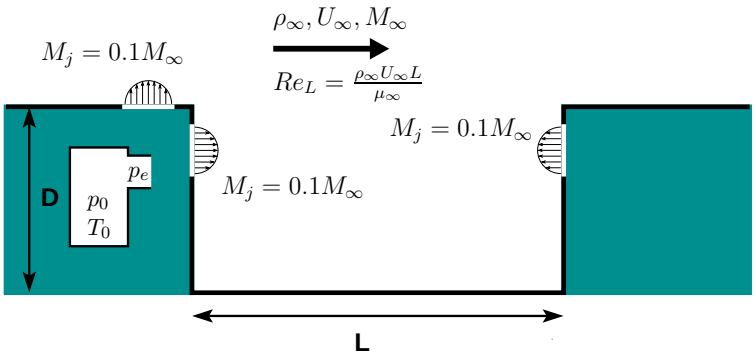


(c) Jet

**Figure 9. Schematics of the spoiler, slanted cavity walls and jet (with steady blowing) at different positions.**

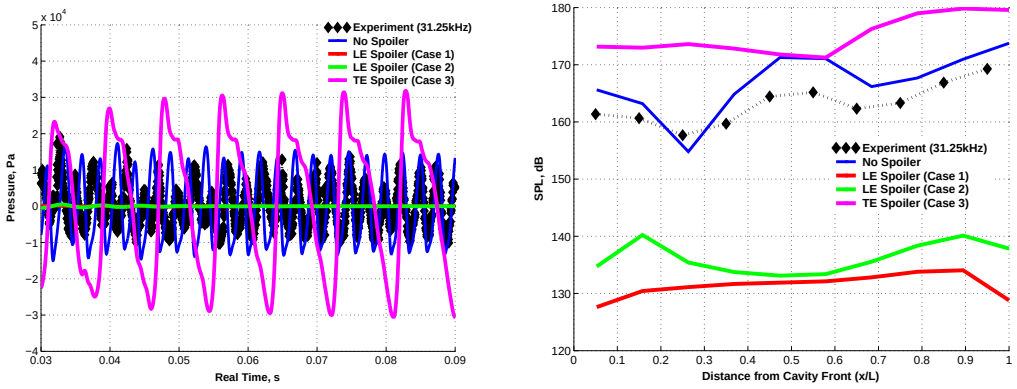


(a) Pressure Traces ($x/L = 0.95$)

(b) SPLs

**Figure 10. Pressure traces (at $x/L = 0.95$) and SPLs along cavity floor of the 2D, L/D=5 cavity using the SST turbulence model with: LE Spoiler (Case 1), LE Spoiler (Case 2), TE Spoiler (Case 3). CFD and experimental results with no spoiler also included.**

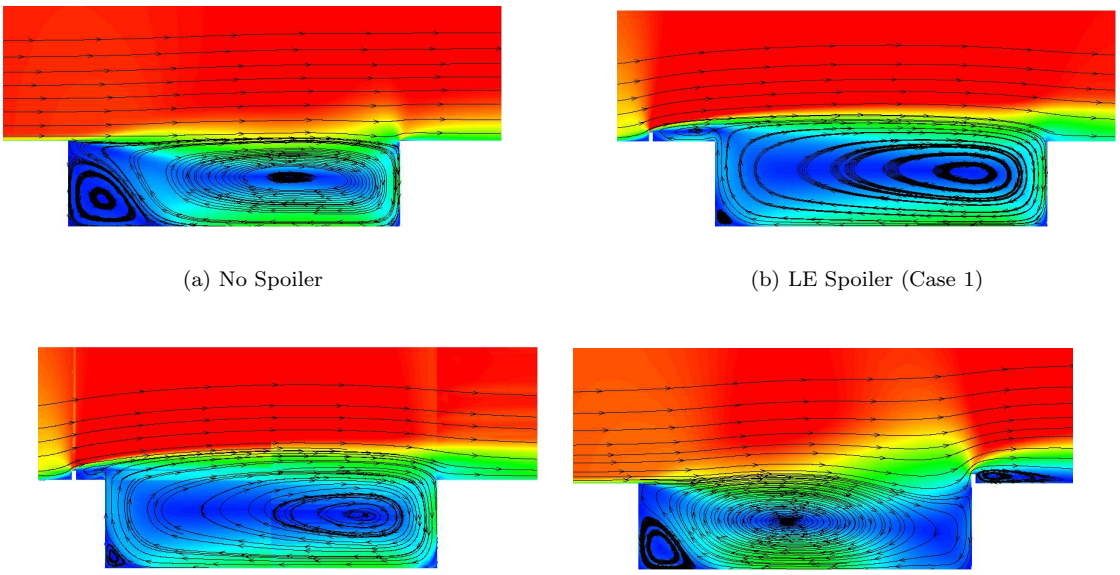

(a) No Spoiler

(b) LE Spoiler (Case 1)

(c) LE Spoiler (Case 2)

(d) TE Spoiler (Case 3)

**Figure 11. Time-averaged Mach contours with streamlines using the SST model for the 2D, L/D=5 cavity with the spoiler upstream and downstream of cavity (see Figure 9(a)). All plots use Mach number normalised with reference to the free-stream Mach number, $M_\infty = 0.85$.**

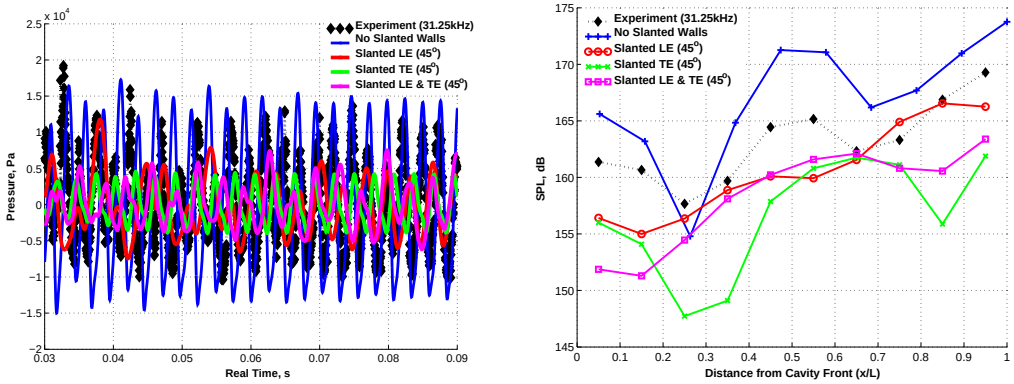


(a) Pressure Traces ($x/L = 0.95$)

(b) SPLs

**Figure 12. Pressure traces (at $x/L = 0.95$) and SPLs along cavity floor for the 2D, L/D=5 cavity using the SST turbulence model for slanted front wall, slanted rear wall and both walls slanted. Slant angle fixed at 45° .**

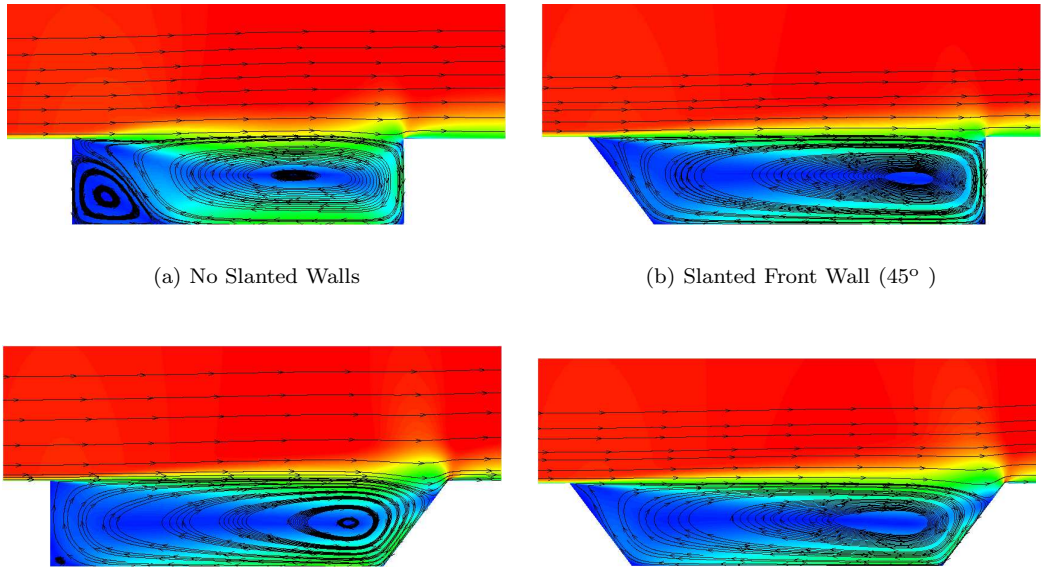

(a) No Slanted Walls

(b) Slanted Front Wall (45° )

(c) Slanted Rear Wall (45° )

(d) Slanted Front & Rear Walls (45° )

**Figure 13. Time-averaged Mach contours with streamlines using the SST model for the 2D, L/D=5 cavity with slanted front wall, slanted rear wall and both walls slanted. Angle of slant kept fixed at 45° .**

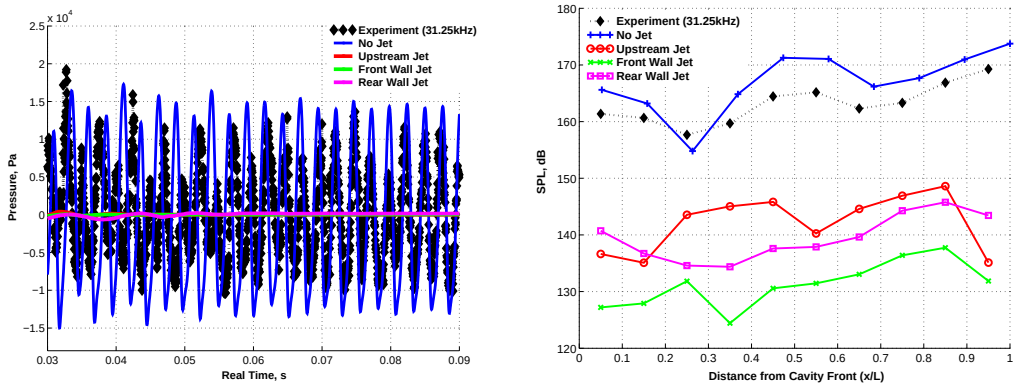


(a) Pressure Traces ($x/L = 0.95$)

(b) SPLs

**Figure 14. Pressure traces (at $x/L = 0.95$) and SPLs along cavity floor for the 2D, L/D=5 cavity using the SST turbulence model with steady jet blowing applied upstream of cavity, at front wall and at rear wall.**

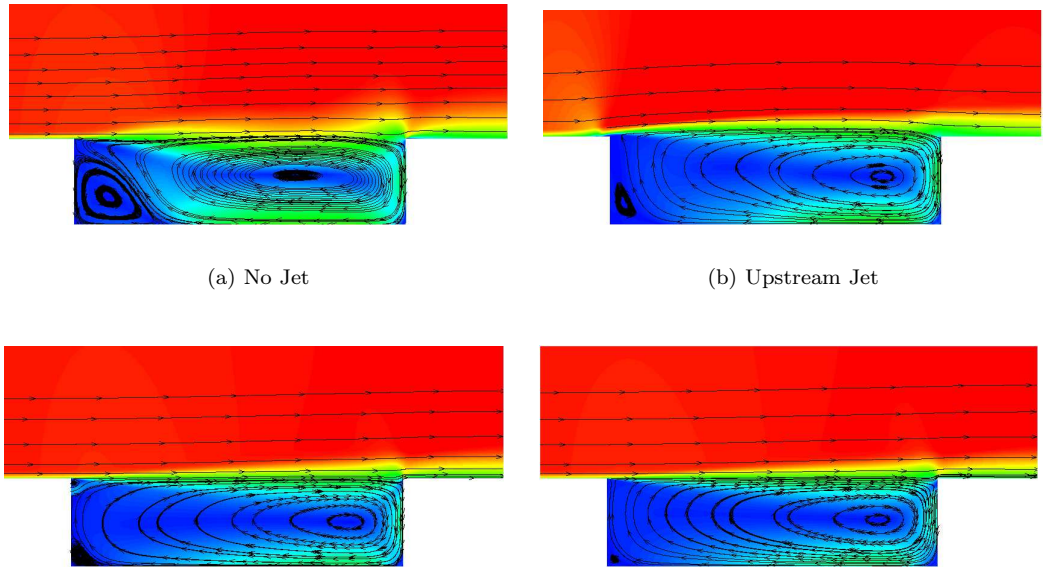

(a) No Jet

(b) Upstream Jet

(c) Front Wall Jet

(d) Rear Wall Jet

**Figure 15. Time-averaged Mach contours with streamlines inside the 2D, L/D=5 cavity using the SST turbulence model with steady jet blowing applied upstream of cavity, at front wall and at rear wall.**